Morphing Blades: Theory and Proof of Principles

Ignazio Maria Viola, Gabriele Pisetta, Weidong Dai, Abel Arredondo-Galeana, Anna M. Young and Amanda S.M. Smyth

Abstract—**Tidal turbines experience large load fluctuations due to the unsteady environment and the shear in the tidal flow. Mitigating these fluctuations without affecting the mean load would result in lower capital and operational costs. In this paper we discuss how this could be achieved through blades that passively and elastically adapt their camber and angle of attack to counteract unsteady flow conditions. Firstly, we discuss the underlying principles of unsteady thrust mitigation. We show that complete cancellation of the thrust fluctuations would be possible if every blade section could pitch passively and independently of neighbouring sections. Secondly, we provide proof of principle for two practical implementations through physical experiments and computational fluid dynamics simulations. We consider a blade that is rigid near the leading edge and flexible near the trailing edge. We show that the unsteady load mitigation is proportional to the ratio between the length of the flexible and rigid parts of the blade. For example, for a blade section where the flexibility is concentrated in a hinge at 3/4 of the chord, the amplitude of the fluctuations is 3/4 of the original amplitude. Secondly, we consider a solid, rigid blade with a passive pitch mechanism. We show that, for a 1 MW turbine operating in shear flow, more than 80% of the unsteady loading is mitigated. These results demonstrate the potential effectiveness of morphing blades for mitigating thrust fluctuations on tidal turbines.**

Index Terms—**Adaptive blades, fatigue, fluid-structure interaction, morphing blades, unsteady aerodynamics.**

I. INTRODUCTION

TIDAL energy is a promising renewable energy source that could critically contribute to energy security [1]. The world's first arrays of tidal turbines (Meygen and Nova's Bluemull Sound, 2016) have only recently been deployed in Scotland. For this energy sector to develop further, new technology must be developed to reduce the levelised cost of energy (LCOE), which is the minimum constant price at which electricity has to be sold in order to break-even over the lifetime of the project. Technology that enables more reliable and cheaper tidal turbines to be built would contribute to a reduction in the LCOE and it would provide more competitive renewable energy.

The large load fluctuations induced by the shear and turbulence of the onset flow, wave-induced current fluctuations, yaw misalignment, interaction with the support structures, and wakes of the upstream devices present a major challenge to the design of tidal turbines [2], [3]. To increase local blockage and thus yields, tidal turbines might be placed in close proximity, resulting in additional unsteady load fluctuations [4]. Load fluctuations are transmitted from the blades to the rest of the turbine making fatigue failures a key limit to reliability [5]. Furthermore, unsteady loads are reflected in power output fluctuations, which result in over-dimensioned power-take-off systems [6] and in a lower maximum mean operating power. Therefore, unsteady load mitigation is critical to reducing LCOE and enhancing the competitiveness of tidal energy.

Load fluctuations are currently mitigated by actively varying the turbine speed, by actively pitching the blades, or by enabling the blade to twist passively to feather when the fluid dynamic load increases (also known as hydroelastic tailoring) [7]. Unfortunately, the effectiveness of these control systems decreases with the size of the blade. Passive twist is currently adopted by Schottel Hydro, whose 70 kW turbines are 6.3 m in diameter. On the other hand, the higher loads on SIMEC Atlantis Energy's MW-scale tidal turbines are incompatible with the flexibility required for passive twist.

Fast-actuated flaps, like those used on aircraft wings, could mitigate higher frequency fluctuations [8]–[10]. These flaps are smaller and therefore could have a faster response than a whole blade pitching system, but they still require electrical power, hinges with bearings and actuator mechanisms that are exposed to debris and biofouling. This additional complexity of the system is seen by industry as posing a risk to turbine reliability. The cost of maintenance of both offshore wind and tidal turbines is a major driver compared

Paper submitted on 31 Dec. 2021, published 29 September 2022.

This work was supported in part by the EPSRC under grants EP/M02038X/1, EP/P007805/1, EP/V009443/1. GP is funded by the CDT grant EP/L016680/1

I.M.Viola, G. Pisetta and W. Dai are with the School of Engineering, Institute for Energy Systems of the University of Edinburgh, Edinburgh, Scotland, EH9 3FB, UK (e-mails: i.m.viola@ed.ac.uk, gabriele.pisetta@ed.ac.uk, w.dai@ed.ac.uk).

A. Arredondo-Galeana was at the School of Engineering, Institute for Energy Systems of the University of Edinburgh, Edinburgh, Scotland, EH9 3FB, UK . He is now at the Department of Naval Architecture, Ocean And Marine Engineering, University of Strathclyde, Glasgow, Scotland, G4 0LZ, UK (e-mail: abel.arredondo-galeana@strath.ac.uk).

A. Young is with the Department of Mechanical Engineering, University of Bath, Bath, BA2 7AY, UK (e-mail: amy32@bath.ac.uk).

A.S.M. Smyth is with the Department of Engineering Science, University of Oxford, Oxford OX1 3PJ, UK (e-mail: amanda.smyth@eng.ox.ac.uk).

Digital Object Identifier: https://doi.org/10.36688/imej.5.183-193

to onshore wind. Hence, reliability is paramount [11]. For example, tidal companies such as Nova Innovation, Nautricity and Schottel Hydro adopt fixed pitch blades to maximise reliability. Orbital Marine Power and SIMEC Atlantis Energy, which operate the largest rotors, only use collective pitch control, which cannot mitigate fast load fluctuations due to, for example, shear, interference, yaw misalignment, etc.

Last year, the European Commission identified blades with built-in chordwise flexibility as one of the most promising concepts for reducing the costs of the blades and the downstream components of turbines [12]. In this paper we discuss the underlying principles of load alleviation through morphing blades and we demonstrate the key conclusions with computational fluid dynamics (CFD) simulations and physical experiments in a water tunnel. 'Chordwise flexibility' or 'morphing' is here defined as a modification to the angle of attack or camber line of the blade, in response to changing inflow conditions. This is commonly done through pitch changes or through trailing-edge flaps.

The rest of the paper is organised as follows. In Section II, the two methods - flexible trailing edges and passive pitch - are introduced and compared in terms of their practical implementation. After this, in Section III, models are derived for the performance of both mechanisms. Numerical and experimental studies into trailing edge flaps and passive pitch are then discussed in Sections IV and V, respectively. Finally, conclusions are drawn.

II. FLEXIBLE TRAILING EDGE VERSUS PASSIVE PITCH

Let us consider a foil that deforms in the chordwise direction, passively and elastically. Such a foil alters its shape by adjusting the camber in response to flow fluctuations. Since the camber determines the angle of zero lift, increasing the camber provides extra lift, whereas decreasing it reduces the lift.

A flexible foil whose shape deformation is continuous along the chord can be conceptually simplified to a rigid foil with a trailing edge flap: a change in the flap angle results in a change in the camber line and thus in the lift. The otherwise distributed flexibility of the foil is lumped together in an angular spring connecting the foil and the flap.

In the limiting condition where the hinge is at the leading edge of the foil, the foil-flap system becomes a single rigid foil that pitches elastically about the leading edge. Hence, a morphing foil could be implemented either as a foil with distributed flexibility, a rigid foil connected to a flap by a spring, or a rigid foil pitching around a sprung axis.

Figure 1 demonstrates two possible practical implementations of the morphing blade concept. In Fig. 1a, we consider a blade that is flexible in the chordwise direction. We assume that the blade sections do not interact with each other but morph independently in response to the local flow conditions. This condition represents either a flexible blade material with low shear modulus and negligible shear stresses between sections, or a series of independent trailing edge flaps along the span. In this paper, we model each section as a rigid foil with a sprung trailing-edge flap. In Fig. 1b, we consider instead a rigid blade sprung to pitch about an axis parallel to the span.

The key idea underpinning both concepts is to consider a spring that, in the mean flow conditions, provides the necessary pitching moment to enable the desired mean hydrodynamic loading. This is achieved with a spring preload, without which a hinged flap (Fig. 1a) or a pitching blade (Fig. 1b) would tend to align itself to the mean flow direction resulting in a lower mean load. By pre-loading the spring, such that the spring moment is equal and opposite to the hydrodynamic moment at the design point, the mean performance of the morphing blade is the same as that of a rigid blade.

In this paper, we will demonstrate the ability of both concepts presented in Fig. 1 to reduce fluctuating blade loads, while maintaining steady performance. First the theoretical background will be outlined, after which experimental and numerical data will be presented.

III. THEORETICAL CONSIDERATIONS

A. Flat Plate Model

We investigate a fixed-pitched plate at non-zero incidence with a flexible trailing edge, which is represented as a flap with a sprung hinge. In the limit of placing the sprung hinge of the flap at the leading edge, the plate would be flat and it would rotate as a rigid body. The hydrodynamic force would vary due to angle of attack variations rather than camber variations. The pitching flat plate is therefore a limiting condition of the fixed-pitch plate with a pitching flap. We will first consider the pitching flat plate, as it allows a more intuitive appreciation of the physics.

B. Mean Flow Conditions

To formalise this concept, consider a rigid plate operating in a steady flow velocity U at an angle of attack $\bar{\alpha}$, see notation in Fig. 2. To ensure that an equivalent plate with a sprung hinge at the leading edge provides the same hydrodynamic force as the rigid plate, the hydrodynamic pitch moment M_h must be equal and opposite to the pitch moment provided by the spring M_κ. For an ideal spring, the moment increases linearly with the deformation, hence

$$M_\kappa = \kappa\theta_0, \tag{1}$$

where θ_0 is the pitch angle resulting from the preloaded spring with stiffness κ.

C. Angle of Attack Variations

Consider now an angle of attack fluctuation $\alpha' = \alpha - \bar{\alpha}$, where $\alpha' \ll \bar{\alpha}$, and let the flow velocity U remain constant. Because the angle of attack variation α' is small, we can assume that the chord-normal force

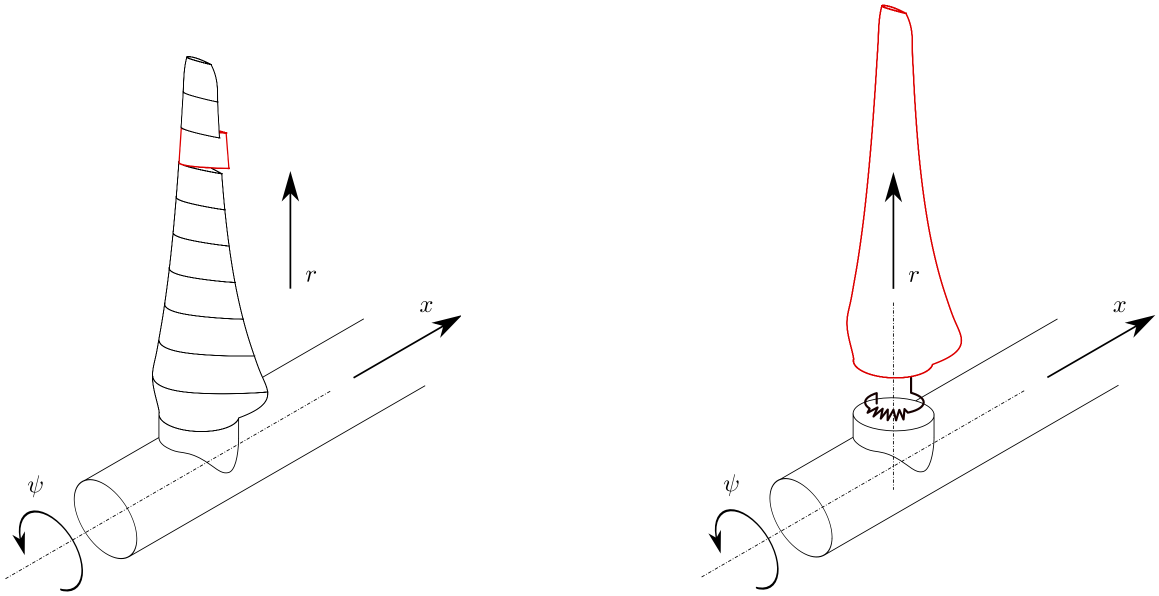

(a) Each section bends independently.

(b) All the sections deflect together.

Fig. 1: Two possible concepts for morphing blades.

N and the moment M_h vary linearly with the angle of attack. Let us define

$$n_\alpha \equiv \frac{\partial N}{\partial \alpha}, \text{ and } m_\alpha \equiv \frac{\partial M_h}{\partial \alpha}, \tag{2}$$

then $N = n_\alpha \bar{\alpha}$ and $M_h = m_\alpha \bar{\alpha}$. For any stiffness κ, we find that the plate deflection δ for an angle fluctuation α' must satisfy the equilibrium condition

$$M_\kappa(\theta_0 + \delta) = M_h(\bar{\alpha} + \alpha' - \delta). \tag{3}$$

Using the slopes κ and m_α, (3) can be written as

$$\kappa(\theta_0 + \delta) = m_\alpha(\bar{\alpha} + \alpha' - \delta), \tag{4}$$

We can now solve for δ recalling that $\kappa(\theta_0) = m_\alpha(\bar{\alpha})$:

$$\kappa\delta = m_\alpha \alpha' - m_\alpha \delta, \tag{5}$$

$$\delta = \frac{m_\alpha}{\kappa + m_\alpha} \alpha'. \tag{6}$$

If $\kappa \to \infty$ then $\delta \to 0$ and the plate is rigid, while if $\kappa \to 0$ then $\delta \to \alpha'$. From Eq. 1, for $\kappa \to 0$ then $\theta_0 \to \infty$ to balance the mean hydrodynamic moment, hence, $\delta \ll \theta_0$. Therefore, $M_\kappa = \kappa(\theta_0 \pm \delta) \approx \kappa\theta_0$, and the restoring moment of the highly flexible spring described above is almost constant. Hence, a highly flexible spring can be replaced by a device providing a constant pitch moment.

For highly flexible springs, the chord-normal force remains constant because

$$N = n_\alpha(\bar{\alpha} + \alpha' - \delta) = n_\alpha(\bar{\alpha}). \tag{7}$$

However, since the plate has changed orientation, the total torque and thrust components on a turbine blade will differ even though the normal force remains constant. Let the pitch β be the angle between the rotor plane and the plate chord. The thrust is $N \cos\beta$. Hence, to achieve a constant thrust, the deflection δ is such that

$$n_\alpha \bar{\alpha} \cos\beta = n_\alpha(\bar{\alpha} + \alpha' - \delta) \cos(\beta + \delta). \tag{8}$$

It is not possible to write an explicit equation for δ, but for $\delta \ll \beta$ such that $\cos(\beta + \delta) \approx \cos\beta$, we find that the displacement $\delta = \alpha'$ would cancel the thrust fluctuations. By substituting this result into, for example, equation (5), we find that the optimum stiffness is $\kappa \to 0$.

It is possible to employ a morphing blade that delivers both a constant thrust and a constant torque. However, this would require a different pitching plate model that is beyond the scope of this paper. In contrast, the present model can mitigate only the principal torque fluctuations. In fact, the torque is given by $N \sin\beta$. Following the same approach as for the thrust, the reader can find that the deflection allowing a constant torque is

$$\delta = \frac{\bar{\alpha} + \alpha' - \beta \pm \sqrt{(\bar{\alpha} + \alpha' - \beta)^2 + 4\alpha'\beta}}{2}. \tag{9}$$

For any α, β and m_α, the optimum stiffness can also be found by substituting this result into equation (5) and rearranging for k:

$$\kappa = m_\alpha \left(\frac{2\alpha'}{\bar{\alpha} + \alpha' - \beta \pm \sqrt{(\bar{\alpha} + \alpha' - \beta)^2 + 4\alpha'\beta}} - 1 \right). \tag{10}$$

In this case, the optimum stiffness depends on the angle of attack fluctuation α', and thus the plate can cancel only the principal fluctuation.

D. Flow Velocity Variations

Now consider both a variation of the angle of attack, $\alpha' = \alpha - \bar{\alpha}$, and of the dynamic pressure, $q' = q - \bar{q}$. As a first approximation, we can consider that the Reynolds number effect is small and, hence, the hydrodynamic forces and moments vary linearly with the dynamic pressure $q = \frac{1}{2}\rho U^2$, where ρ is the fluid density and U

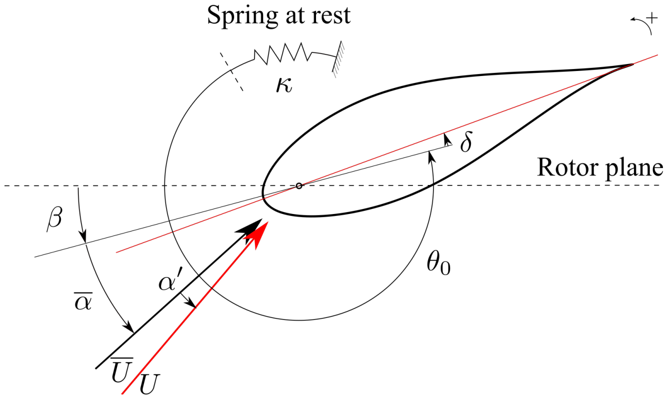

Fig. 2: Passively pitching foil.

the flow velocity. We linearise the hydrodynamic force and moment such that

$$\begin{aligned} N(\alpha, q) &= N(\bar{\alpha}, \bar{q}) + n_\alpha \alpha' + n_q q' \\ M_h(\alpha, q) &= M_h(\bar{\alpha}, \bar{q}) + m_\alpha \alpha' + m_q q', \end{aligned} \tag{11}$$

where

$$n_q \equiv \frac{\partial N}{\partial q}, \text{ and } m_q \equiv \frac{\partial M_h}{\partial q}. \tag{12}$$

Then, the equilibrium between spring and hydrodynamic moments is

$$\kappa(\theta_0 + \delta) = M_h(\bar{\alpha}, \bar{q}) + m_\alpha(\alpha' - \delta) + m_q q'. \tag{13}$$

Noting that, in static conditions, $\kappa\theta_0 = M_h(\bar{\alpha}, \bar{q})$, we rearrange (13) to find:

$$\kappa\delta = m_\alpha \alpha' - m_\alpha \delta + m_q q', \tag{14}$$

$$\delta = \frac{m_\alpha}{k + m_\alpha}\alpha' + \frac{m_q}{k + m_\alpha} q', \tag{15}$$

$$\delta = \frac{1}{\frac{\kappa}{m_\alpha} + 1}\left(\alpha' + \frac{m_q}{m_\alpha} q'\right). \tag{16}$$

If $\kappa \to \infty$ then $\delta \to 0$ and the plate is rigid, while if $\kappa \to 0$ then $\delta \to \alpha' + (m_q/m_\alpha)q'$. From potential flow theory, we find that the aerodynamic centre is fixed at the quarter chord. As the arm of the moment is constant, $m_q/m_\alpha = n_q/n_\alpha$, and for highly flexible springs the normal force N remains constant for any angle and flow velocity fluctuation. In fact, the chord-normal force during a gust is

$$\begin{aligned} N(\alpha, q) &= N(\bar{\alpha}, \bar{q}) + n_\alpha(\alpha' - \delta) + n_q q' \\ &= N(\bar{\alpha}, \bar{q}) + n_\alpha \left(\alpha' - \left(\alpha' + \frac{n_q}{n_\alpha} q'\right)\right) + n_q q' \\ &= N(\bar{\alpha}, \bar{q}), \end{aligned} \tag{17}$$

which is the same as for the average angle of attack $\bar{\alpha}$ and the average dynamic pressure $\bar{q}$. As shown in section III-C, cancelling the normal force variations will almost entirely cancel the thrust fluctuations, and it is possible to cancel the normal force variations with an infinitely flexible spring (see discussion after Eq. 8).

For example, Fig. 3 shows the effect of varying spring stiffness on the fluctuations of the sectional thrust coefficient C_x for a blade section at 75% of the span of a horizontal-axis, axial-flow, 1 MW turbine with a diameter $D = 18$ m [13]. The hub is mounted 20 m above the seabed and 20 m below the free surface. The pitching plate model and blade element momentum theory (BEMT) are solved analytically for a tip speed ratio $\lambda = 4.5$ in a stream of $U = 2$ ms^{-1} at the hub height. The rotation through the shear flow, which is described by a 1/7 power law, results in a periodic variation of both α and q. When $\kappa \to \infty$ (dark red), the blade section has a fixed pitch and it experiences large fluctuations. As the spring becomes more flexible, κ decreases and the amplitude of C_x fluctuations is gradually reduced to zero. The optimum is found for a very flexible spring. For $\kappa \to 0$ (dark blue), the fluctuations increase by a comparatively small amount in the opposite direction.

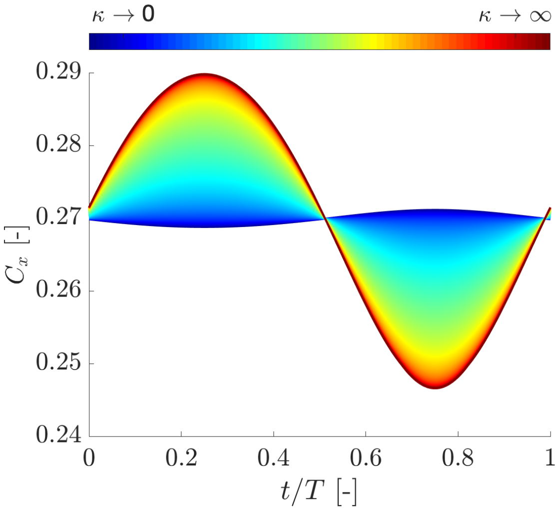

Fig. 3: Sectional thrust coefficient C_x over a nondimensional period of revolution t/T of a morphing blade section at 75% of the span of a 1 MW turbine operating at a tip speed ratio of 4.5 in shear flow. The colours indicate the stiffness of the spring of the morphing blade section, from rigid (dark red) to flexible (dark blue).

E. Flat Plate with a Flap

To model a morphing blade with a pre-loaded trailing-edge flap, we use a quasi-steady panel model representation. The foil is represented by two panels, one for the main body and one for the flap, each with an associated vortex located at 1/4 of the length of each panel, giving the foil circulation (Γ). Collocation points cp$_1$ and cp$_2$, where the boundary conditions are evaluated, are located at 3/4 of the length of each panel. Figure 4 illustrates the panel model and associated dimensions. The distance from the leading edge to the flap hinge is denoted x_p, while the flap length is denoted a.

To obtain an expression for the circulation strength of each panel vortex, we first consider the case of an undeflected trailing edge flap ($\delta = 0$, Fig. 4a). Applying the boundary condition of zero flow normal to the surface at each collocation point, we obtain the following from the Biot-Savart law:

$$\text{cp}_1 : \frac{\Gamma_1}{2\pi r_{11}} - \frac{\Gamma_2}{2\pi r_{21}} = -U\sin(\alpha) \approx -U\alpha \tag{18}$$

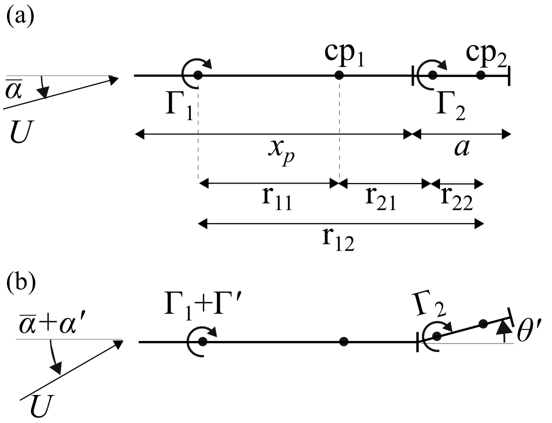

Fig. 4: Schematic diagram of the panel method used to model a flat plate with a flap, shown at the mean angular position in (a) and the deflected position in (b).

$$\mathrm{cp}_2 : \frac{\Gamma_1}{2\pi r_{12}} + \frac{\Gamma_2}{2\pi r_{22}} = -U\sin(\alpha) \approx -U\alpha \tag{19}$$

Here r_{mn} denotes the distance from the vortex at panel m to the collocation point on panel n. Considering now a small increase in angle of attack α' (Fig. 4b), the low stiffness of the pre-loaded spring ensures that the moment M_k on the trailing-edge flap is approximately constant (see section III-C), which in turn means that the circulation of the flap panel, Γ_2, is constant. Applying the boundary condition again, we obtain the following:

$$\mathrm{cp}_1 : \frac{\Gamma_1 + \Gamma_1'}{2\pi r_{11}} - \frac{\Gamma_2}{2\pi r_{21}} \approx -U(\alpha + \alpha') \tag{20}$$

$$\mathrm{cp}_2 : \frac{\Gamma_1 + \Gamma_1'}{2\pi r_{12}} + \frac{\Gamma_2}{2\pi r_{22}} \approx -U(\alpha + \alpha') + U\delta \tag{21}$$

By substituting Eq. 18 and 19 into Eq. 20 and 21, and solving for Γ_1', we obtain:

$$\Gamma_1' = -2\pi r_{11} U \alpha' \tag{22}$$

Noting that Γ_2 is constant and thus cannot contribute to unsteady loading, the change in lift L' resulting from the change in angle of attack can be obtained from Eq. 22. Since $r_{11} = x_p/2$, this gives the unsteady force as:

$$L' = -\rho U \Gamma_1' = 2\pi U^2 \rho \frac{x_p}{2} \alpha' \tag{23}$$

$$C_L' = 2\pi\alpha' \frac{x_p}{c} \tag{24}$$

Comparing this to the load experienced by a fully rigid foil ($2\pi\alpha'$), the unsteady load reduction is:

$$2\pi\alpha' - 2\pi\alpha' \frac{x_p}{c} = 2\pi\alpha'\left(1 - \frac{x_p}{c}\right) = 2\pi\alpha' \frac{a}{c} \tag{25}$$

Thus, the unsteady load reduction obtained from the pre-loaded trailing edge flap is given by the flap to chord ratio a/c. In the limiting case of $a = c$ (i.e. a rigid flat plate rotating about its leading-edge), the unsteady lift will cancel completely.

IV. EXPERIMENTAL AND NUMERICAL STUDY OF PASSIVE TRAILING-EDGE FLAPS

As described in Section III-E, one way to change the camber of a foil both passively and elastically is to employ a flap connected to the foil by a hinge with a spring. In this section, we present the results of experiments undertaken in a water tunnel with free surface (i.e. a flume) and computational modelling of a 2D NACA-0012 profile with and without a trailing-edge flap hinged at 75% of the foil chord.

A. Experimental Method

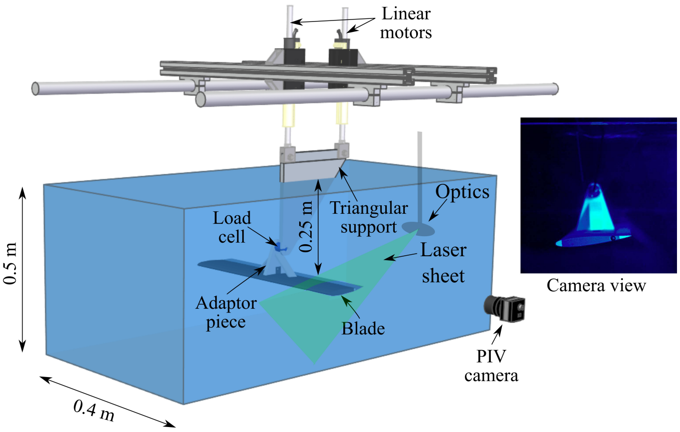

Fig. 5: Schematic diagram of the experimental setup to test the foil with flap in the water tunnel. The camera view shows the morphing model at its equilibrium position.

Tests are performed in a free surface water tunnel at the School of Engineering, the University of Edinburgh (Fig. 5). The water tunnel is $9\,\mathrm{m}$ long, and $0.4\,\mathrm{m}$ wide. The mean water depth is set to $0.5\,\mathrm{m}$ and the model is placed horizontally $0.25\,\mathrm{m}$ below the water surface.

We test two foils, both with chord $c = 0.1\,\mathrm{m}$ and span $S = 0.39\,\mathrm{m}$. The spanwise gap between the model and the lateral wall of the tunnel is $5\,\mathrm{mm}$ on each side. The foils are identical except that one is rigid, whereas the other has a hinge placed at 75% of the chord so that the final part of the foil acts as a flap. The flap and the foil are connected with a shaft and six ball bearings. The foils are 3D printed in PLA material.

As discussed in Sec. III-A (see discussion after Eq. 8), the maximum alleviation of the unsteady thrust is achieved for a spring with high preload angle and low stiffness, such that the pitching moment provided by the spring is constant. Hence, an approximately constant pitch moment is exerted on the trailing edge flap to ensure that the mean position of the flap coincides with that of the trailing edge of the solid foil.

Whist this would not be possible on a rotating blade, in our laboratory setting where the foil is fixed and horizontal (Fig. 5), we can achieved a constant moment by exploiting the flap buoyancy. In fact, the buoyancy of the flap is a constant upwards force. Because the flap fluctuations (θ') are small, the constant buoyancy force results in an approximately constant moment on the hinge. It must emphasised that this is not a suitable means to exert a constant moment on a rotating blade with a trailing edge flap. Further details on the experiments are provided by Arredondo-Galeana et al. [14].

The experimental rig consists of two linear motors that transmitted a heaving motion to the model. The foils are connected to a load cell, which is connected to an adaptor piece that held the foil into place (see camera view in Fig. 5). Load cell measurements are sampled at 1000 Hz and data is acquired for 100 cycles in each test. Experiments are carried out at $Re = 50,000$ and results are phase averaged. To verify the experimental setup, the steady lift coefficient C_L of the rigid foil at different angles of attack is compared with that measured by Sheldahl and Klimas [15] at $Re = 50,000$ for the same foil shape (Fig. 6).

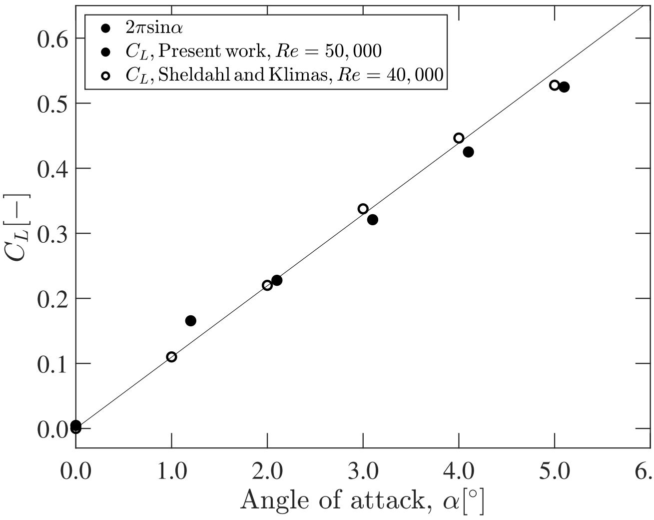

Fig. 6: Lift coefficient C_L of the rigid foil measured at different values of the angle of attack in steady conditions and comparison with values measured by Sheldahl and Klimas [15] and those predicted by thin airfoil theory ($C_L = 2\pi \sin\alpha$).

The kinematics of the models are given by

$$h = h_0 e^{i\omega t} \qquad \dot{h} = i\omega h_0 e^{i\omega t} \qquad \ddot{h} = -\omega^2 h_0 e^{i\omega t}. \quad (26)$$

It has been shown that the gusts encountered by tidal turbines are typically in the reduced frequency range $0 < f_r < 0.6$ [16], [17] and that gusts due to regular waves result in angle of attack amplitude oscillations of the order of 5° [17]. In this work, three peak-to-peak heaving amplitudes ($2h_0/c = 0.1, 0.3, 0.5$) and three reduced frequencies ($f_r = 0.1, 0.3, 0.5$) are selected as representative of the tidal environment. The mean angle of attack is set to 5°, and these testing conditions correspond to amplitudes of the angle of attack oscillations of 0.6° to 14.0°. The larger angle of attack variations are intended to test limits of the validity of the model proposed in Section III-A, which assumes small angle oscillations and attached flow conditions.

B. Numerical Method

The Reynolds-averaged Navier-Stokes equations for incompressible flow and Newtonian fluids are solved in STAR-CCM+. We use a realizable $k-\epsilon$ two-equation turbulence model and a weakly coupled fluid structure interaction approach. A second order implicit finite difference Newmark-Wilson scheme is used to approximate at every j-th time step of size Δt, the angular acceleration $\ddot{\beta}$, the angular velocity $\dot{\beta}$ and the angular position β of the flap (and, in Sec. V, of the whole blade):

$$\ddot{\beta}_j = \frac{M_{\mathrm{k}_j} + M_{h_{j-1}}}{I}, \quad (27)$$

$$\dot{\beta}_j = \dot{\beta}_{j-1} + \frac{1}{2}\left(\ddot{\beta}_j + \ddot{\beta}_{j-1}\right)\Delta t, \quad (28)$$

$$\beta_j = \beta_{j-1} + \dot{\beta}_{j-1}\Delta t + \frac{1}{4}\left(\ddot{\beta}_N + \ddot{\beta}_{j-1}\right)\Delta t^2, \quad (29)$$

where I is the moment of inertia, M_h is the hydrodynamic moment and M_k is the spring moment.

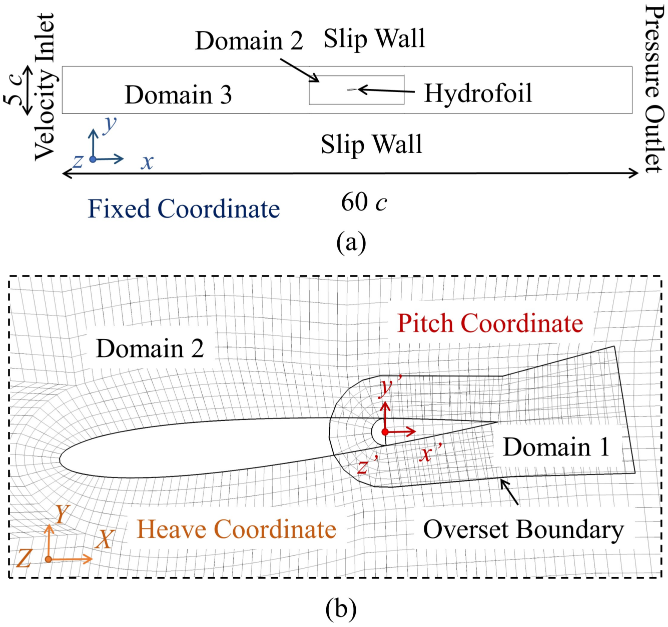

Fig. 7: (a) Background computational domain and, (b) inner computational domain and grid.

Figure 7 shows the two-dimensional computational domain and the block non-orthogonal structured grid. Domain 3 represents the water tunnel and it is meshed with an H-Type grid. It is $60c$ in length and $5c$ in height. The length is longer than the water tunnel to allow prescribing a uniform velocity and pressure at the inlet and outlet boundaries, respectively. Conversely, the height corresponds to the water depth in the water tunnel. The bottom wall of the water tunnel and the free surface are modelled as rigid boundaries with a slip velocity. This condition accurately represents the experimental condition on the bottom boundary because the displacement boundary layer thickness in the water tunnel is negligible and thus the displacement of the streamlines due to the boundary layer can be neglected. The free surface is modelled as rigid because the free surface does not deform noticeably during the experiments.

Domain 2, which is inside of Domain 3 and is meshed with a C-Type grid, extends five chords upstream and seven chords downstream of the foil. It is $3c$ in height and it is connected to Domain 3 through a morphing interface. Domain 1 is an overlapping C-Type grid around the flap. Domain 1 and 2 heave periodically with respect to the inertial reference system fixed with the water tunnel (x, y, z). In addition, Domain 2 rotates around the Z axis of the heaving coordinate system (X, Y, Z). The pitch angle, velocity and acceleration are calculated by Equations 27-29. The grid in Figure 7 is made of 1.2×10^4 cells and it has an average y^+ of around 50 at the solid boundaries, thus requiring the use of wall functions. To assess the numerical uncertainty, we test two finer grids by halving the grid size twice, as well as three time steps: $0.005c/U$, $0.01c/U$ and $0.05c/U$. Following the uncertainty quantification process proposed by Viola et al. [18], the numerical uncertainty due to the grid and time resolution for ΔC_L is estimated in $\pm 10\%$.

C. Results

Figure 8 shows the measured ΔC_L for rigid and passive flap foils at $f_r = 0.1, 0.3, 0.5$. The three tested displacement amplitudes, $2h_0/c = 0.1, 0.3, 0.5$, are identified with blue, red and black markers, respectively. The measurements of rigid and passive flap foils are plotted with cross and circular markers, respectively. In the figure, the solid line shows ΔC_L predicted by Theodorsen's theory, whilst the solid-dotted line the one predicted by the analytical model presented in Sec. III-E.

For all measurements, the circular markers of the passive flap foil are below the cross markers of the rigid foil. The percentage alleviation is about 25% for most of the tested cases, except for most extreme cases $2h_0/c = 0.5$ and $f_r = 0.3, 0.5$, where the amplitude of the angle of attack oscillations increases above $10°$ and load alleviation drops to about 15%. At these high angle of attack oscillations, dynamic stall becomes dominant and we do not expect the model of Sec. III-E to work. This is confirmed at the most extreme cases of Fig. 8, where the measured ΔC_L shows lower load alleviation than the one predicted by the model. Further details on the interaction between flap and vortex flow due to dynamic stall can be found in Arredondo-Galeana et al. [14].

In Table I, the load alleviation predicted by the CFD simulations is compared with the experimental data for two different frequencies and amplitudes of motion. It can be seen that the simulations and experiments agree within their respective error bands. As both the cases considered are away from dynamic stall, the load alleviation achieved is around the 25% predicted by the inviscid model in Section III-A. This agreement between the CFD and experiments gives confidence that CFD could be used to investigate the load alleviation potential over a wider parameter space or for other gust/foil motions if required.

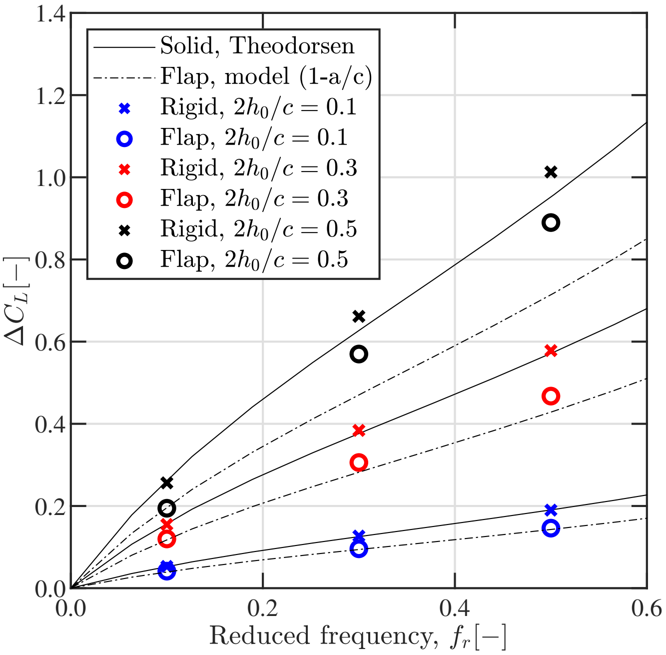

Fig. 8: Amplitude of the lift coefficient fluctuations (ΔC_L) of the rigid foil and that with a passive flap at three reduced frequencies, $f_r = 0.1$, 0.3 and 0.5 and three heaving displacements $2h_0/c = 0.1$, 0.3 and 0.5. The experimental uncertainty of the measured ΔC_L is ± 5%. The solid line shows ΔC_L predicted by Theodorsen's theory, whilst the solid-dotted line the one predicted by the model presented in Sec. III-E.

TABLE I: Amplitude of the lift coefficient fluctuations (ΔC_L) of the rigid foil and that with a passive flap predicted by CFD and experiments. Uncertainty is indicated for the 95% confidence level.

$f_r = 0.1$ $2h_0/c = 0.3$	$\Delta C_{L_{\text{Rigid}}}$	$\Delta C_{L_{\text{Morphing}}}$	Relative Reduction
CFD	0.16 ± 10%	0.11 ± 10%	31%
EXP	0.16 ± 5%	0.12 ± 5%	25%

$f_r = 0.3$ $2h_0/c = 0.1$	$\Delta C_{L_{\text{Rigid}}}$	$\Delta C_{L_{\text{Morphing}}}$	Relative Reduction
CFD	0.12 ± 10%	0.09 ± 10%	25%
EXP	0.13 ± 5%	0.10 ± 5%	23%

V. NUMERICAL AND ANALYTICAL STUDY OF PASSIVELY-PITCHING TURBINE BLADES

In this section, we present the results of a numerical and analytical study on the 1 MW, 3-blade 18-m-diameter turbine described in Sec. III-D, operating in a shear onset flow with $U = 2$ ms^{-1} at hub height. We consider both fixed-pitch blades as well as rigid blades that can passively pitch around an axis parallel to the span as shown in Fig. 1b.

To identify the optimum spring stiffness and preload that maximise unsteady thrust mitigation, we use an analytical implementation of the pitching plate model presented in Sec. III-A-D coupled with a BEMT formulation. This is the same model underlying the results in Fig. 3. The values for stiffness from the analytical-BEMT model are also used in the CFD model described in the following section.

A. Numerical method

The solver and fluid-structure-interaction approach described in Section IV-B is used for these simulations. Figure 9 shows the computational domain, the geometry, and the hexahedral block non-orthogonal structured grid of approximately 23 million cells in total. The turbine is meshed within an inner cylindrical domain, which rotates inside a stationary cuboid domain $17D \times 11D \times 2D$, where D is the diameter of the turbine.

The two domains are coupled by a sliding internal interface, updated at every time step. The grids near the blade deform to enable the change in blade pitch. Figure 9c shows the gap of 2 mm between the blade and the hub to allow the blade to pitch. Figure 9d-e show the C-O grid topology adopted for the blade. The blade surface is meshed with a grid size of $0.015c$ both streamwise and spanwise, while the wall-normal grid size results in $y^+ = 70$. The boundary layer is thus modelled with a wall function.

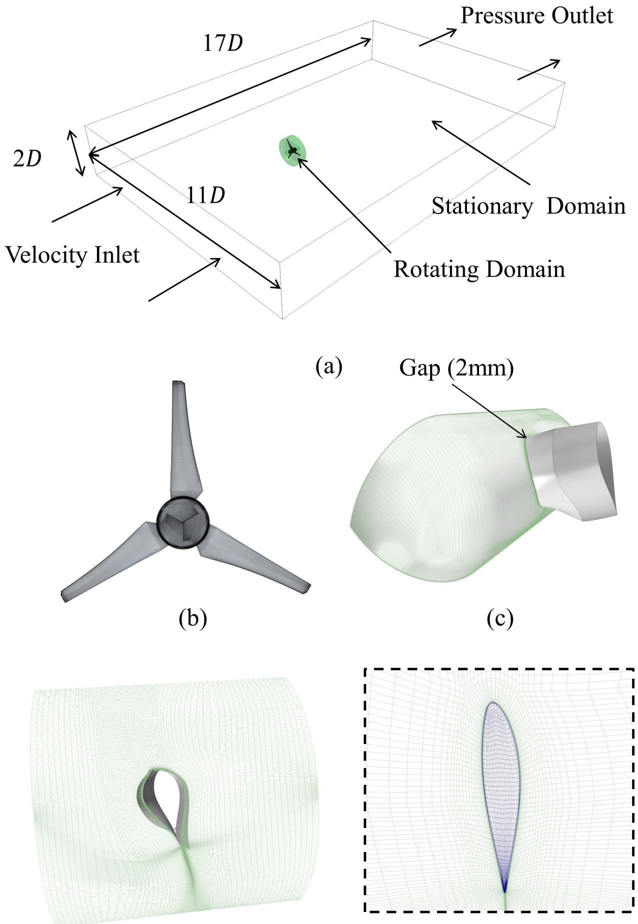

(a) (b) (c) (d) (e)

Fig. 9: Numerical setup of the CFD simulations of the rotor: (a) computational domain and boundary conditions; (b) surface grid of the rotor; (c) surface grid at the hub-rotor interface; (d) grid around a thick section of the blade near the root, and (e) around a thin section near the tip.

The numerical uncertainty is estimated by modelling with the same grid and time resolution the fixed blade tested by [19] at $Re = 2 \times 10^6$ at the NASA Ames Wind Tunnel. Three grids are tested by doubling and halving the grid size, spanning y^+ values between 50 and 100. Three time steps are also considered: $0.0006c/U$, $0.003c/U$ (reference value) and $0.015c/U$. Following the uncertainty quantification process proposed by Viola et al. [18], the uncertainty is estimated in $\pm 10\%$ for both the fluctuation in thrust coefficient ΔC_X and tangential force coefficient ΔC_ϕ.

Figure 9a also shows the boundary conditions. A 1/7 power law is used at the velocity inlet such that each blade experienced load fluctuations with a period T of one per revolution. A constant reference pressure is set on the pressure outlet. A slip-velocity condition is employed for the rest of the outer surfaces of the stationary domain, while a no-slip condition is used on the blade and hub surface.

B. Results

The power and thrust coefficient (C_P and C_T, resp.) for the fixed-pitch blade turbine computed with BEMT and CFD are reported in Fig. 10. These are also compared with the CFD results of Gretton and Ingram [13] for the same turbine. The highest C_P is reached at the tip-speed ratio $\lambda = 4.5$, which is thus used in the rest of the paper.

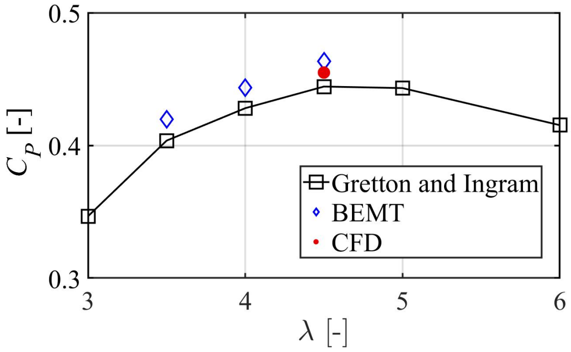

(a) Power coefficient.

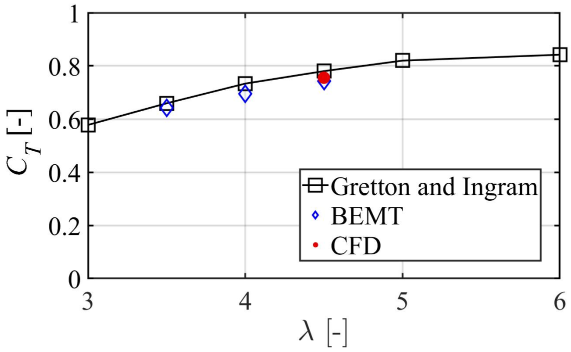

(b) Thrust coefficient.

Fig. 10: Power (C_P) and thrust (C_T) coefficient of the rotor with three fixed-pitch blades versus the tip-speed ratio (λ) predicted with BEMT and CFD, and comparison with the CFD results by Gretton and Ingram [13].

The flow field is characterised by the strong tip and hub vortices, visualised in Fig. 11 by isosurfacses of the Q-criterion. The differences between the rotor with fixed (Fig. 11a) and passive (Fig. 11b) pitch blades are negligible for these vortical structures.

At this optimum tip speed ratio, flow separation occurs over a small region on the suction side of the blades near the hub. This is shown in Fig. 12a and 12b for the fixed and passive pitch respectively. The blade is pictured at different azimuthal positions and the color shows the region on the suction side of the blade where the tangential wall shear stress is negative and thus the boundary layer is separated. The figure clearly shows that the passive pitch does not prevent flow separation for this blade design and optimum λ. However, it mitigates the already small variations in the contour of the separated flow region between the different azimuthal positions.

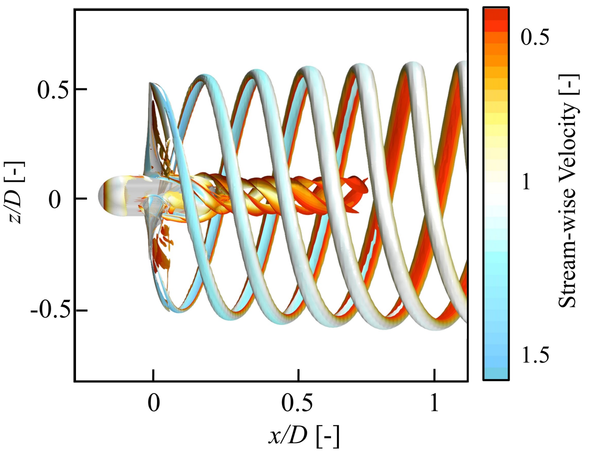

(a) Fixed-pitch blade rotor.

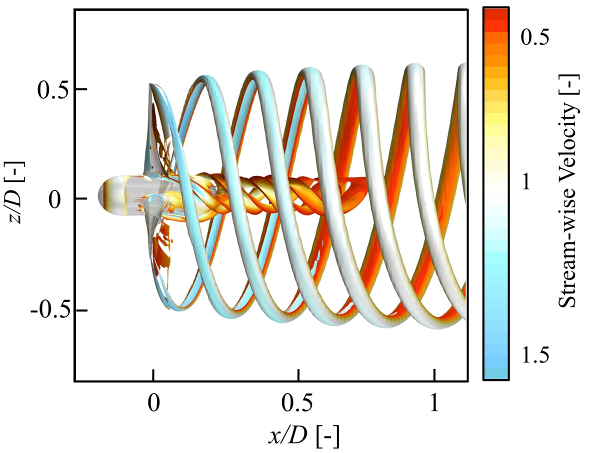

(b) Passive-pitch blade rotor.

Fig. 11: Isosurfaces of nondimensional Q-Criterion, $Q = 20$, colored by nondimensional streamwise velocity for the rotor equipped with (a) fixed and (b) passive pitch blades. The Q-criterion and the velocity are nondimensionalised using U_{hub} and D.

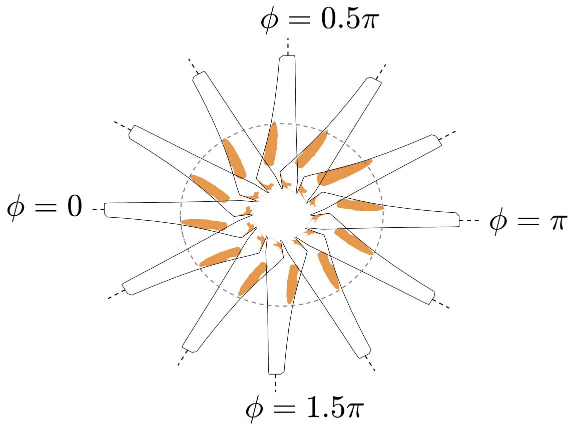

(a) Fixed pitch blade.

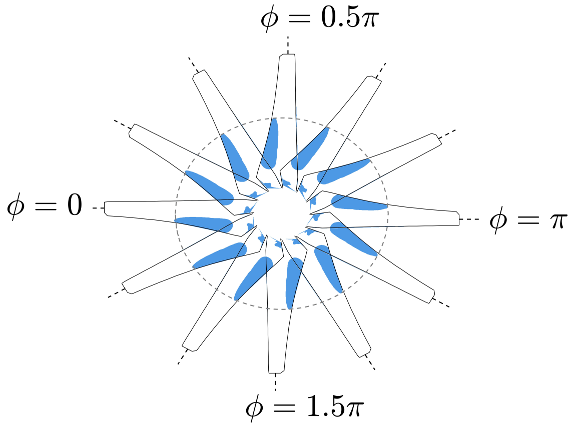

(b) Passive pitch blade.

Fig. 12: Suction side of the blade at different azimuthal positions with colored regions of where the tangential wall shear stress is negative and thus the boundary layer is separated.

In contrast, the effect of the passive pitch is significant on the forces experienced by the blades. Figure 13 shows, for a single blade, the thrust coefficient C_X in the streamwise direction, and the tangential force coefficient C_ϕ within the rotor plane, for one blade. It is noted that the rotor trust coefficient C_T shown in Fig. 10b is the time average of C_X. Both data calculated with the analytical model and phased-averaged CFD results are presented. The solid lines show the results for a fixed pitch blade and the dashed lines show those for a passive pitch blade. Both methods predict that the passive pitch allows more than 80% unsteady load reduction without affecting the mean load, and thus the fatigue loading is reduced without any loss in the mean power extracted.

The same results are summarised in Table II, where it can be seen that the CFD and the analytical-BEMT model agree on the load reduction, despite some discrepancies in the prediction of the unsteady load amplitudes that are within the numerical uncertainty (10% at 95% confidence level). In particular, the BEMT model appears to over-predict the unsteady loading on the rigid blade; this may be due to the limitations of the BEMT model in capturing 3D effects in unsteady flow [20].

If each blade section were equipped with an optimal spring stiffness, and inertia and damping were negligible, complete load mitigation could be achieved. In the present case, instead, the spring is optimised in a global fashion and thus the fluctuations are minimised only for the sections that most contribute to the thrust. Furthermore, the fluid and blade inertia, and the viscous damping reduce the unsteady load mitigation. The inertia and the damping are also responsible for the phase shift observed in Fig. 13 between the fixed and passive pitch blades.

Finally, it is noted that although the system is optimised to mitigate thrust, the torque fluctuations are also reduced by 27% (CFD) or 35% (BEMT). While beyond the scope of this paper, passive blade concept can be modified to minimise torque fluctuations as well as thrust fluctuations. In contrast, in this paper we focus on the simpler passive blade concept aiming at minimising thrust fluctuations (see Section III-C for a discussion of why torque fluctuations are more complex to mitigate).

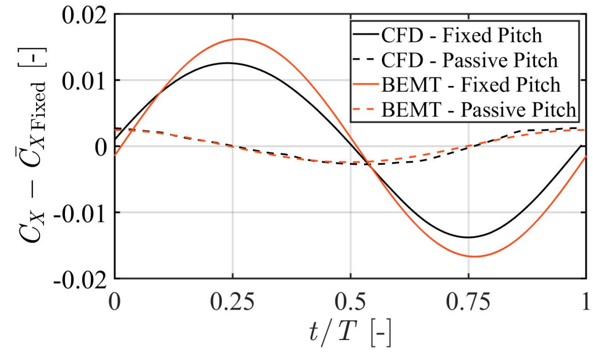

(a) Thrust coefficient.

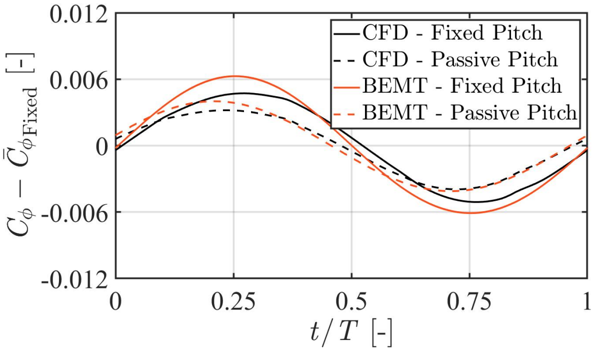

(b) Tangential force coefficient.

Fig. 13: Phased-averaged thrust coefficient C_X (a) and tangential coefficient C_ϕ (b) versus the nondimensional time t/T predicted with CFD and BEMT. The mean of the thrust ($\bar{C}_{X\,\mathrm{Fixed}}$) and tangential ($\bar{C}_{\phi\,\mathrm{Fixed}}$) force coefficients are subtracted to highlight the differences in the amplitude of the oscillations.

TABLE II: Thrust (ΔC_X) and tangential force (ΔC_ϕ) amplitude of rigid and passive pitch blade predicted by CFD and BEMT.

	$\Delta C_{X_{\mathrm{Rigid}}}$	$\Delta C_{X_{\mathrm{Passive}}}$	Relative Reduction
CFD	0.0132 ± 10%	0.0027 ± 10%	80%
BEMT	0.0164	0.0024	83%

	$\Delta C_{\phi_{\mathrm{Rigid}}}$	$\Delta C_{\phi_{\mathrm{Passive}}}$	Relative Reduction
CFD	0.0049 ± 10%	0.0036 ± 10%	27%
BEMT	0.0062	0.0040	35%

VI. CONCLUSIONS

This paper summarises progress in the formulation and proof of principle of the morphing blade concept, which enables a reduction in the unsteady-loading for tidal turbines, improved resilience and reliability, and a reduction in the levelised cost of energy. Tidal turbines operate in a turbulent, sheared, unsteady flow resulting in large load fluctuations. These can lead to fatigue failures of the blades and to power fluctuations. Cancelling the load fluctuations would allow higher fatigue life and the use of a lower rated generator for the same mean power output.

In contrast to the well-understood passive spanwise twist concept, which is widely adopted in the wind industry to pitch the blade to feather during a gust, we consider chordwise deformations. The blade deforms passively and elastically. We consider two morphing blades concepts: (1) a blade with a fixed pitch and a flexible trailing edge, which we model as a flap with lumped flexibility at the hinge; (2) a rigid blade with a passive, elastic pitch mechanism. We model both concepts with the same analytical framework.

We present an analytical model of the morphing blade and we identify the optimal stiffness (i.e. the torsional spring or trailing edge stiffness). We show that the mean moment exerted by the optimal torsional spring is large compared to the moment fluctuations, and thus the spring moment can be substituted by a constant pitch moment. This is important because it can significantly simplify the practical implementation.

In the case of a fixed-pitch blade with a trailing edge flap connected through a spring, the amplitude of the fluctuations can be decreased only up to the ratio between the chord length of the flap and of the entire foil. For example, if the flap is hinged at 3/4 of the blade chord, the amplitude of the fluctuations is 3/4 of the original amplitude. We demonstrate the above analytical findings with computational fluid dynamics simulations and with physical experiments in a water tunnel.

Complete unsteady load cancellation would be possible if each blade section could be equipped with an optimal spring and if it could pitch independently of the other sections. However, we show that significant unsteady load mitigation can be achieved by adopting one globally optimum spring for all sections, and by locking all sections together. In particular, we model a 1 MW turbine in shear flow with both blade element momentum theory and with a blade-resolved computational fluid dynamics simulation, and we show that rigid blades passively pitching around the spanwise axis enable a reduction of over 80% in the thrust fluctuations and of 25% in the torque fluctuations.

Overall, this paper explains the underlying mechanisms underlying the mitigation of thrust fluctuations through a morphing blade, and demonstrates practical implementations enabling unsteady load amplitude reductions between 25% and 80%.

ACKNOWLEDGEMENT

The authors are grateful to Susan Tully, Robin LeMestre and Gabriel Scarlett for their preliminary

work on morphing blades.

REFERENCES

[1] D. Cagney, R. Gruet, and Ocean_Energy_Europe, "Powering Homes Today, Powering Nations Tomorrow," ETIP Ocean, Tech. Rep., 2019.

[2] G. T. Scarlett, B. Sellar, T. van den Bremer, and I. M. Viola, "Unsteady hydrodynamics of a full-scale tidal turbine operating in large wave conditions," *Renewable Energy*, vol. 143, pp. 199–213, 2019.

[3] G. T. Scarlett and I. M. Viola, "Unsteady hydrodynamics of tidal turbine blades," *Renewable Energy*, vol. 146, pp. 843–855, 2020.

[4] C. R. Vogel and R. H. Willden, "Improving Tidal Turbine Performance Through Multi-Rotor Fence Configurations," *J. Mar. Sci. Appl.*, vol. 18, no. 1, pp. 17–25, 2019.

[5] B. Murray, S. Leen, and C. M. O Bradaigh, "Void distributions and permeability prediction for rotationally moulded polymers," *J. Mater. Des. Appl.*, vol. 229, no. 5, pp. 403–418, 2015. [Online]. Available: http://pil.sagepub.com/lookup/doi/10.1177/1464420714525135

[6] F. Scuiller, T. Tang, Z. Zhou, M. Benbouzid, and J. Fre, "A review of energy storage technologies for marine current energy systems," *Renew. Sustain. Energy Rev.*, vol. 18, pp. 390–400, 2013.

[7] T. Barlas and G. van Kuik, "Review of state of the art in smart rotor control research for wind turbines," *Progress in Aerospace Sciences*, vol. 46, no. 1, pp. 1–27, 2010.

[8] T. Barlas and M. Lackner, "Smart rotor blade technology applied to the Upwind reference turbine," in *IEA Top. Expert Meet. Appl. smart Struct. large Wind turbine rotor Bl.*, Sandia National Labs, Alberquerque, USA, 2008.

[9] T. K. Barlas, G. J. van der Veen, and G. A. M. Kuik, "Model predictive control for wind turbines with distributed active flaps: incorporating inflow signals and actuator constraints," *Wind Energy*, vol. 15, pp. 757–771, 2012.

[10] A. Young, J. Farman, and R. Miller, "Load alleviation technology for extending life in tidal turbines," in *Progress in Renewable Energies Offshore-Proceedings of 2nd International Conference on Renewable Energies Offshore, RENEW 2016*, 2016, pp. 521–530.

[11] A. MacGillivray, H. Jeffrey, C. Hanmer, D. Magagna, A. Raventos, and A. Badcock-Broe, "Ocean Energy Technology: Gaps and Barriers," Tech. Rep., 2013. [Online]. Available: www.si-ocean.eu

[12] D. Magagna *et al.*, "Workshop on identification of future emerging technologies in the wind power sector," Joint Research Centre, European Commission's science and knowledge service, Tech. Rep. March, 2018.

[13] G. I. Gretton and D. M. Ingram, "Development of a computational fluid dynamics model for a horizontal axis tidal current turbine," The University of Edinburgh, Tech. rep. for the PerAWAT project, 2011.

[14] A. Arredondo-Galeana, A. Young, A. Smyth, and I. M. Viola, "Unsteady load mitigation through a passive trailing edge flap," *Journal of Fluid and Structures (submitted)*, 2021.

[15] R. E. Sheldahl and P. C. Klimas, "Aerodynamic characteristics of seven symmetrical airfoil sections through 180-degree angle of attack for use in aerodynamic analysis of vertical axis wind turbines," *Sandia National Laboratories.*, 3 1981.

[16] C. L. Sequeira and R. J. Miller, "Unsteady gust response of tidal stream turbines," in *2014 Oceans - St. John's*, Sep. 2014, pp. 1–10.

[17] G. T. Scarlett and I. M. Viola, "Unsteady hydrodynamics of tidal turbine blades," *Renewable Energy*, vol. 146, pp. 843 – 855, 2020.

[18] I. M. Viola, P. Bot, and M. Riotte, "On the uncertainty of CFD in sail aerodynamics," *Int. J. Numer. Methods Fluids*, vol. 72, pp. 1146–1164, 2013.

[19] R. Piziali, "2-d and 3-d oscillating wing aerodynamics for a range of angles of attack including stall," 1994.

[20] A. S. M. Smyth and A. M. Young, "Three-dimensional unsteady hydrodynamic modelling of tidal turbines," *EWTEC proceedings*, 2019.